SHEARLESS AND SHEARED FLOW PAST A CIRCULAR CYLINDER: COMPARATIVE ANALYSIS BY MEANS OF LES

Takeshi Omori, Suad Jakirlić and Cam Tropea
Fachgebiet Strömungslehre und Aerodynamik, Technische Universität Darmstadt
Petersenstr. 30, D-64287 Darmstadt, Germany
t.omori@sla.tu-darmstadt.de, s.jakirlic@sla.tu-darmstadt.de, ctropea@sla.tu-darmstadt.de

Shinnosuke Obi
Department of Mechanical Engineering, Keio University
Hiyoshi 3-14-1, Kohoku-ku, Yokohama 223-8522, Japan
obsn@mech.keio.ac.jp

ABSTRACT

Large Eddy Simulation (LES) of the uniform shear flow past a circular cylinder at Reynolds number $Re_D = 3900$ with increasingly enhanced mean shear magnitude $|du_F/dy|$ corresponding to the shear rate ($SR = |du_F/dy|D/u_F$) range between 0 (shear less flow) and 0.177 have been performed in order to provide a basis for comparative analysis of the shear-induced effects with respect to the structural characterization of the cylinder wake. An important outcome arising from the present computational study relates to the assymmetric shape of the mean quantity profiles with the local maxima/minima shifted to the high velocity side, indicating a strong modulation of the large scale structures in the wake due to the imposed mean shear. It applies especially to the far wake region. Here, the structures illustrated by the fluctuating pressure field clearly show their existence only on the high velocity side. In contrast, the small scale structures remain almost unaffected by the mean shear.

INTRODUCTION

One of the most frequently investigated flow configurations in the fluid mechanics research in general is certainly the flow past a circular cylinder. Because of its fundamental importance (it represents a generic configuration for studying vortex dynamics, the drag and lift variation due to wake unsteadiness, etc.) and its relevance in technical applications this flow has been intensively investigated in the past, see e.g. a review of early works on this topic in Hinze (1975) up to some recent computational studies, e.g., Breuer (1998) and Travin et al. (1999). In all these works the oncoming flow was uniform, i.e. with no mean shear imposed. However, flow situations where the oncoming flow exhibits a strong velocity gradient are more likely encountered in industrial practice. This is especially valid if the cylinder is situated in the wall vicinity characterized by strong velocity variation. The present work deals with such a flow. According to the authors' awareness there are just a few studies dealing with a flow past a sphere/cylinder subjected to mean shear. The experimental study by Moraga (1999; $Re_D \leq 17000$) showed that the lift force on a sphere has a strong dependence on the Reynolds number and the mean shear intensity of the oncoming flow. This work is followed by a RANS study of the flow past a circular cylinder performed by Basara et al. (2003). All other works, as e.g. that of Legendre and Magnaudet (1997; $Re_D \ll 1$), are related to very low Reynolds number flows. The present fundamental study is pertinent to the disperse phase in solid/liquid upward duct flow and a (nominally) two dimensional circular cylinder (Fig. 1) is considered here rather than a three dimensional, spherical particle. This research aims solely at an in-depth analysis of the structural characterization of the cylinder wake under the conditions of mean shear imposed on the oncoming flow. The study of the wake structure influence on the shear-induced lift force is the topic of a companion work of the same authors (see Omori et al., 2007). The investigated range of the shear parameter, $0 < SR \leq 0.177$, was selected in order to cover the conditions investigated experimentally by Moraga et al. (1999) for which the sign change (from positive to negative) of the lift coefficient occurs.

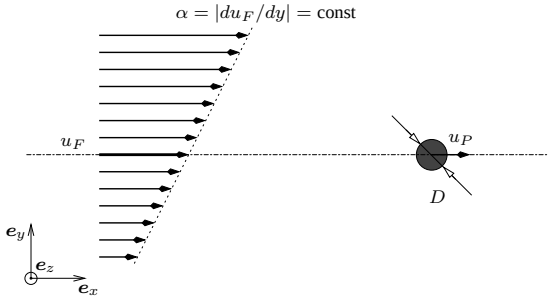

Figure 1: Schematic of the considered flow and the coordinate definition

COMPUTATIONAL METHOD

All simulations were performed with the in-house computer code FASTEST which is based on a finite volume numerical method for solving three-dimensional, filtered Navier-Stokes equations on block-structured, body-fitted, nonorthogonal meshes. Block interfaces are treated in a conservative manner, consistent with the treatment of inner cell faces. A cell centered (collocated) variable arrangement and cartesian vector and tensor components are used. The well-known SIMPLE algorithm was applied for coupling the velocity and pressure fields. The convective transport of all variables was discretized by a second-order central differencing scheme, whose stability was enhanced through the so-called deferred correction approach. Time discretization was accomplished applying the 2nd order (implicit) Crank-Nicolson method. The filtered Navier-Stokes equations governing the incompressible, unsteady flow past a circular cylinder read ($\partial\overline{u}_i/\partial x_i = 0$):

$$\frac{\partial\overline{u}_i}{\partial t} + \overline{u}_j\frac{\partial\overline{u}_i}{\partial x_j} = -\frac{1}{\rho}\frac{\partial\overline{p}}{\partial x_i} + \frac{\partial}{\partial x_j}\left(2\nu\overline{S}_{ij} - \tau_{ij}\right) \quad (1)$$

Table 1: Summary of the grid characteristics

Grid	No. of grid cells $(x-y,z)$	Domain $L_x \times L_y \times L_z$	Near-Wall Resolution $(\Delta x^+_{\max}, (\Delta y^+/2)_{\max}, \Delta z^+_{\max})$	$(\overline{\Delta}/\eta)_{\max}$
A	21043×32	$(-8D, 15D) \times (-5D, 5D) \times (0, \pi D)$	$(20, 0.32, 81)$	22.6
B	34100×32	$(-5D, 18D) \times (-5D, 5D) \times (0, \pi D)$	$(23, 0.32, 78)$	13.1
C	34100×64	$(-5D, 18D) \times (-5D, 5D) \times (0, \pi D)$	$(23, 0.32, 40)$	11.9

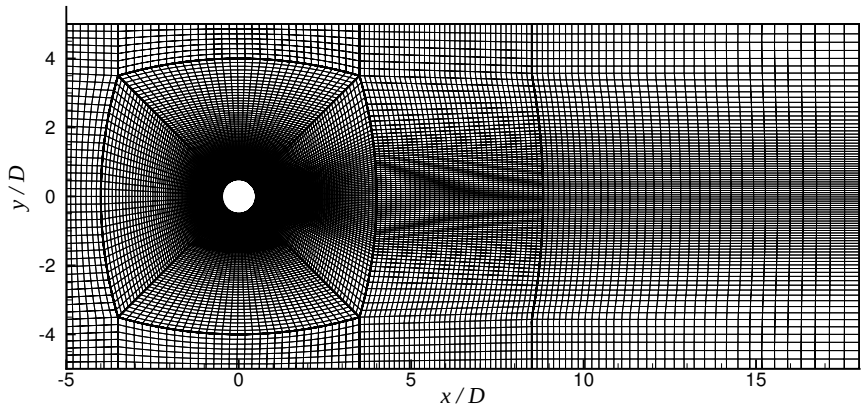

Figure 2: Block and cell distribution for grid B

The quantity $\tau_{ij}(= \overline{u_i u_j} - \overline{u}_i \overline{u}_j)$, called SGS (Sub-Grid-Scale) stress tensor, being the consequence of the filtering procedure, has to be determined by an SGS model. In the present work the most widely used model formulation due to Smagorinsky based on the eddy viscosity assumption is used:

$$\tau_{ij} = -2\nu_t \overline{S}_{ij} + \delta_{ij}\tau_{kk}/3 \qquad (2)$$

The subgrid-scale viscosity ν_t is given by a mixing length model $\nu_t = (C\overline{\Delta})^2 \left|\overline{S}\right|$ with $\left|\overline{S}\right| = \sqrt{2\overline{S}_{ij}\overline{S}_{ij}}$ and $\overline{\Delta} = \sqrt[3]{\Delta x \Delta y \Delta z}$ representing the velocity $(C\overline{\Delta}\left|\overline{S}\right|)$ and length scales $(C\overline{\Delta})$ of the residual (SGS) motion. The model coefficient C was either set to the constant value 0.1 or was dynamically determined by the procedure proposed by Germano et al. (1991) and Lilly (1992). The focus in the present work was on the dynamic procedure.

Computational details

The solution domain adopted was meshed with a block-structured grid, whose topology is displayed in Fig. 2. Three different grids consisting of approximately 670 thousand (grid A), 1.1 million (grid B) and 2.2 million cells (grid C) were used to minimize uncertainties arising from the grid quality. Table 1 gives an overview about the solution domain dimensions with respect to the position of the domain boundaries and appropriate grid resolutions in all three coordinate directions. Fig. 2 shows the plane view of the second finest grid (B), which has higher resolution in the wake region than the coarsest grid (A). The finest grid (C) has the same resolution in the $x-y$ plane as the grid B but doubled number of the grid cells in the spanwise direction. In the case of all three grids, the computational domain was uniformly meshed in the spanwise direction.

Both spanwise dimension and spanwise resolution are in line with some reference LES simulations, as e.g. with those performed by Kravchenko and Moin (2000) and Breuer (1998). In the work of Breuer an O-type grid with domain radius up to $15D$ was used (let us recall that our outlet boundary was positioned at the same distance from cylinder), enabling larger solution domain in cross direction and especially in front of the cylinder, but keeping similar grid resolution. The total number of grid points was approximately the same. Contrary to the grid size around the cylinder itself and in the near wake, which was of the comparable resolution, the far wake was meshed by somewhat more grid cells in the work of Breuer. These circumstances can explain to some extent the differences between present and reference computational results (see section 'Results and Discussion').

No-slip boundary conditions were applied on the cylinder surface and the integration up to the wall was performed. The periodicity of the flow was assumed in the spanwise direction of the domain. At the inlet plane no perturbations were added to the mean velocity profile. The convective boundary conditions given by

$$\frac{\partial u_i}{\partial t} + U_\infty|_{y=0} \frac{\partial u_i}{\partial x} = 0 \qquad (3)$$

was imposed at the outflow plane, the convective velocity corresponding to the mean streamwise velocity U_∞ of the bulk flow taken at the centerline ($y = 0$).

The statistics were accumulated over a period of at least 12 vortex shedding cycles (in most cases the sampling period corresponded to 30 vortex shedding cycles). The spatial averaging was accomplished in the statistically homogeneous spanwise direction. The statistics were monitored at a point placed in the separated shear layer behind the cylinder after every time step and were considered to be converged to the uncertainty of a few percent. The CFL number, representing the time step chosen, did not exceed the unity value in the entire solution domain for the grids B and C. Further time step refinement corresponding to the $CFL \approx 0.5$ did not result in any noticable change. In the case of the coarsest grid, the maximum CFL number was around 2.

The maximum values of the grid spacing in all three coordinate directions are listed in Table 1 along with those for the other two grids. According to the grid resolution criteria for attached flows estimated by Piomelli and Chasnov (1996) which requires the values $\Delta x^+ < 50$ (at most 150), $\Delta y^+ < 2$, $\Delta z^+ < 15$ (at most 40), the near-wall resolution of the grid B seems to be insufficient in the spanwise direciton.

This motivated a further grid refinement by doubling the number of the cells in the z-direction (grid C).

One of the important measures for the grid quality assesment is the ratio of the representative grid scale $\overline{\Delta}$ to the Kolmogorov length scale η. Fig. 3 depicts its variation along the centerline behind the cylinder. The maximum values of this normalized filter width in the entire solution domain is listed in Table 1.

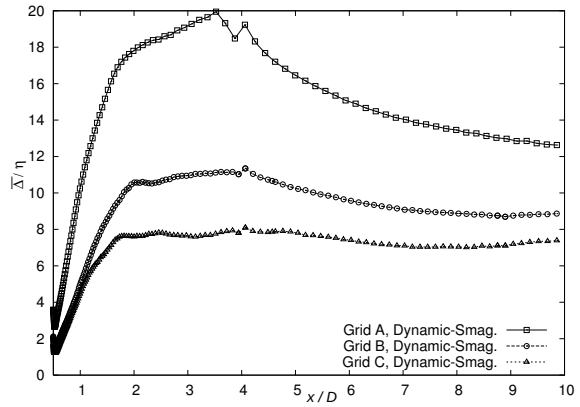

Figure 3: Variation of the filter width normalized by Kolmogorov length along the centerline in the cylinder wake

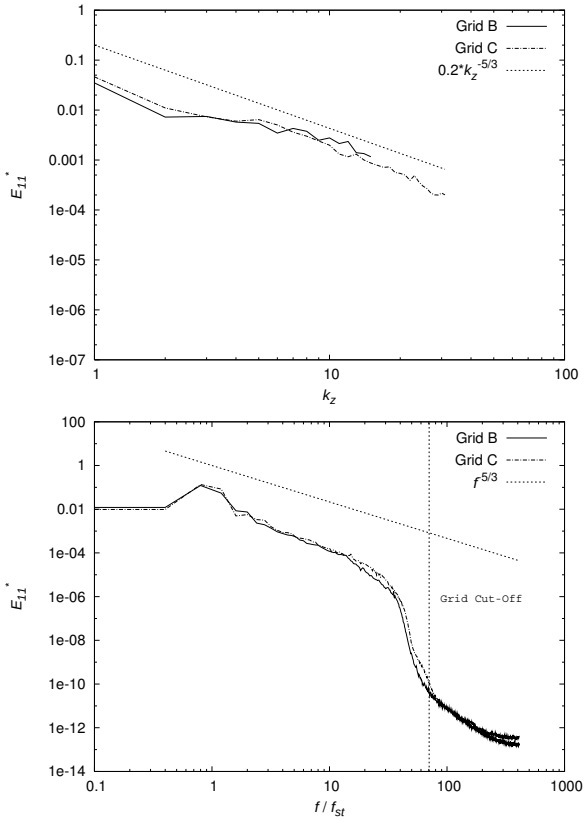

Figure 4: One-dimensional spectra in the wake (the vertical line shows the grid cut-off)

The Kolmogorov length scale η $(= \left(\nu^3/\epsilon\right)^{\frac{1}{4}})$ was evaluated from the dissipation rate as follows with

$$\epsilon \approx \epsilon_{GS} + \mathcal{T}_{GS} = 2\nu\overline{S}_{ij}\overline{S}_{ij} + \tau^a_{ij}\overline{S}_{ij}, \qquad (4)$$

Here ϵ_{GS} and $\mathcal{T}_{GS}$ represent the dissipation rate at the grid scale and the energy transfer rate from the grid scale to the subgrid scale respectively.

Ideally, the filter width should be placed in the inertial subrange. This condition is fulfilled if its size corresponds approximately to 12η, Pope (2000). Obviously the characteristic filter width corresponding to both grids B and C satisfies this constraint, as shown in Table 1 and Fig. 3

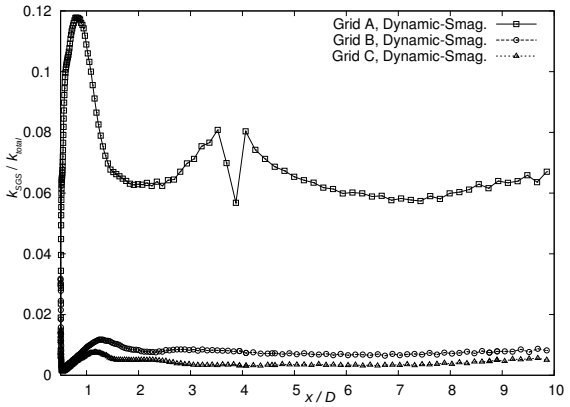

Figure 5: Variation of k_{SGS}/k_{total} along the centerline in the cylinder wake

The spatial and temporal spectra shown in Fig. 4 were measured at the position $x/D = 1.54$, $y/D = 0.5$ for approximately five vortex shedding cycles. A regular decay of slope close to $-5/3$ is observed and the inertial subrange is well resolved, which is essential for a successful LES computation. The Strouhal frequency f_{st}, extracted from the history of the lift coefficient (not shown here), led to the $St = 0.236$. It should be noted that the sampling rate corresponding to the chosen time step width ($f/f_{st} \approx 400$, Fig. 4) is higher than the grid cutoff frequency, the latter denoting the maximal resolvable frequency on the adopted grid in accordance with the streamwise spacing and Taylor's hypothesis. This confirms a sufficient temporal resolution of the present simulations is hiermit confirmed. Fig. 5 (kinks associated with the grid A correspond to the block interface position) displays the SGS contribution to turbulence kinetic energy along the centerline behind the cylinder. This analysis shows a minor contribution to the total k-value (less than 1%) for both grids B and C. The modelled SGS kinetic energy is estimated as $k_{sgs} = \nu_t|\overline{S}|/0.3$, Mason and Callen (1985). The employed resolution maintains the ratio of turbulent SGS viscosity to molecular viscosity under 0.5 (not shown here).

According to this analysis it is concluded that the grid B is appropriate for the present study and can be adopted for further simulations.

RESULTS AND DISCUSSION

To investigate the shear effects and the corresponding wake structure on the cylinder, the simulations were conducted applying the grid B for five different shear rates SR between 0 and 0.177. The Reynolds number was kept constant ($Re_D = 3900$). The dynamic Smagorinsky model was applied as the subgrid scale model. The statistics were sampled over 35 vortex shedding cycles. In the following discussions, the symbol for the filter operation $\overline{(\,)}$ is omitted for the sake of brevity. The evolution of the mean flow and turbulent quantity profiles in the cylinder wake will be shown first for both shear less and sheared cases followed by the analysis of the mean shear influence on the structural properties in the cylinder wake.

Mean flow and turbulence evolution

Fig. 6 displays the profiles of the mean velocities in the wake of cylinder for the shearless case ($SR = 0$). In addition to the present results obtained by both Smagorinsky and dynamic models and available experimental data, the LES results of Breuer (1998) and Kravchenko and Moin (2000) are shown for comparison. The results for the velocity field exhibit a high level of agreement with results of both experiments and reference simulations in both characteristic flow zones: flow reversal immediate behind the cylinder and recovery region. It is also visible in Fig. 7, where the centerline velocity evolution is depicted exhibiting negative values in the separation bubble and gradual increase until the bulk velocity is recovered.

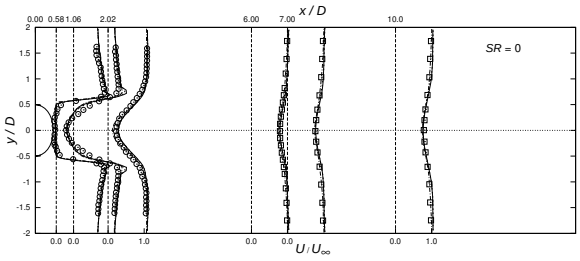

Figure 6: Evolution of the mean axial velocity profiles in the cylinder wake for $SR = 0$

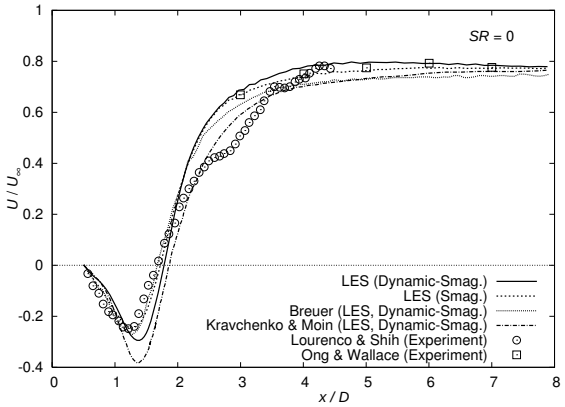

Figure 7: Evolution of the centerline velocity in the cylinder wake for $SR = 0$

Figs. 8 and 9 show the axial velocity and Reynolds stress component development in the cylinder wake corresponding to the highest considered shear rate $SR = 0.117$. The results obtained for the shearless case are also shown in order to emphasize the relative difference between both flow configurations.

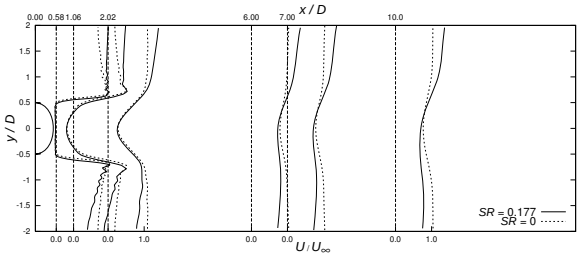

Figure 8: Evolution of the mean axial velocity profiles in the cylinder wake for $SR = 0$ and $SR = 0.177$

The strong asymmetry of the turbulence structure in the far wake is also reflected in the Reynolds stress budget. Fig. 10 compares the redistribution process of the Reynolds shear stress $\langle u'v' \rangle$ along $x/D = 6.0$ for the shearless case and the most strongly sheared case. In both cases, the redistribution term is mostly in balance with the production term but its effect is totally different. While for the shearless case, the redistribution term acts to reduce the level of the Reynolds shear stress and hence the anisotropy, for the sheared case, the redistribution term in fact increases the Reynolds shear stress and causes consequently the shift of other stress components.

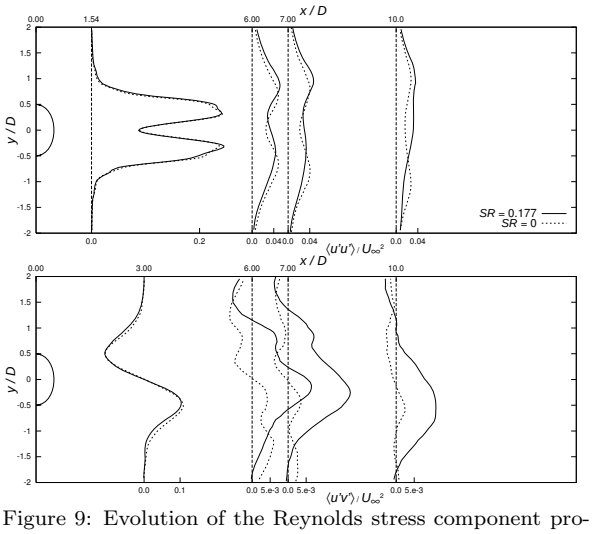

Figure 9: Evolution of the Reynolds stress component profiles in the cylinder wake for $SR = 0$ and $SR = 0.177$

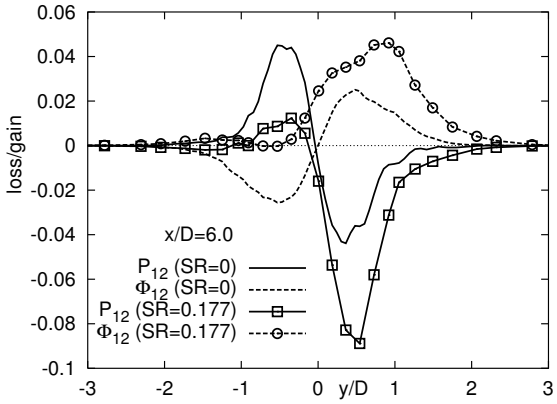

Figure 10: Production (P_{12}) and redistribution (Φ_{12}) terms (normalized by U_∞^3/D) in budget of the equation for the Reynolds shear stress at $x/D = 6.0$

It is interesting to note that the recirculation zone was not affected by the mean shear imposed on the flow. The size of the backflow region was not changed at all. The free reattachment point occurs at $x/D \approx 1.8$. Hence, the profiles in the separation bubble retain their symmetrical shape. The effects of the shear rate imposed is noticable in the regions above (intensification of the convective transport) and below this region and especially in the far wake. The profiles of all quantities become gradually asymmetrical towards the high velocity side. The strongest influence of the mean shear is observed at the profiles of the shear stress component $\langle u'v' \rangle$. The turbulent shear stress exhibits positive values over a wide range of the far wake. Hereby, the positive peak values are substantially higher then the negative ones.

Fig. 11 shows the contours of the mean pressure field with velocity gradient imposed on the oncoming flow. The stagnation point at the upstream cylinder side is clearly shifted towards high velocity flow region, whereas the near wake structure remains nearly symmetrical. The mean pressure distributions on the cylinder for all investigated shear rates are shown in Fig. 12. The normalization was performed us-

ing the reference velocity and reference pressure at the inlet plane at $y/D = 0$ in accordance with the following formulation: $C_p = p - p_\infty/(0.5\rho {U_\infty}^2)$. The angular position was measured clockwise from the stagnation point (intersection of the x axis with the cylinder perimeter). Beside stagnation point displacement the pressure distribution indicates the surface pressure enhancement at the higher velocity side and decrease at the lower velocity side. Apart of that, the pressure coefficient variation reveals almost entirely symmetrical distribution along the downstream cylinder surface ($|\theta| > 100^o$). Another interesting observation is the base pressure coefficient increase in terms of the shear rate enhancement and the consequent drag coefficient decrease (not shown here).

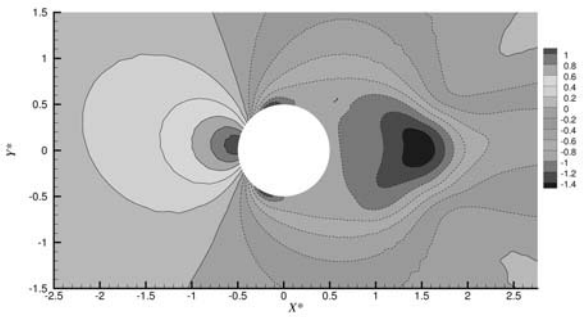

Figure 11: Mean pressure field for $SR = 0.177$

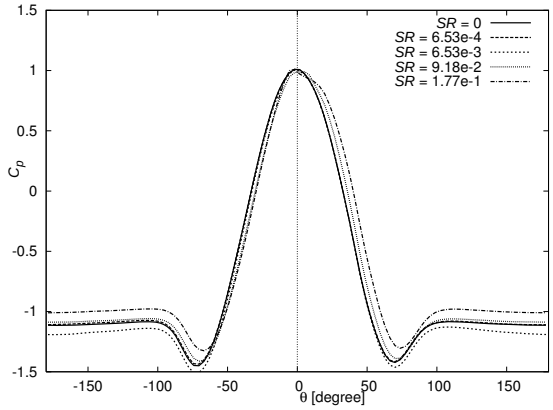

Figure 12: Pressure coefficient distribution around cylindrical particle

Fig. 13 shows the pathlines extracted from the mean velocity field for three typical shear rates. The goal was to explore the origin of the fluid elements which reside within the recirculation zone or flow through it. The pathlines were calculated by integrating back (against the flow directions) the positions of the fluid particles which ended up at the cross-section corresponding to the position $x/D = 0.5$. The pathline plot illustrates the fluid elements on the low velocity side flowing back to the cylinder in the presence of the high shear rate, whereas they recirculate within the separation bubble in the shearless case. Because the fluid elements on the low velocity side posses less momentum, the pressure gradient between the cylinder rear and the ambient wake can be smaller (smaller pressure loss due to recirculation), too. This explains the higher base pressure (Figs. 11 and 12) by enhanced shear rates.

Wake structure behind cylinder

The cylinder wake and its structural characterization have important impact on the forces acting on cylinder. Fig. 14 shows the contours of the instantaneous spanwise vorticity ω_z in the near wake of both shearless and sheared cases. The snapshots were made at the time instant where the lift coefficient reached its minimum. In both flow configurations, the boundary layer separating from the cylinder surface and the consequent development of the Kármán vortex street are clearly promoted. In the sheared case, the shear layer on the lower side tends to be drawn back to the cylinder. This case is characterized by more detailed small structures immediately behind the cylinder.

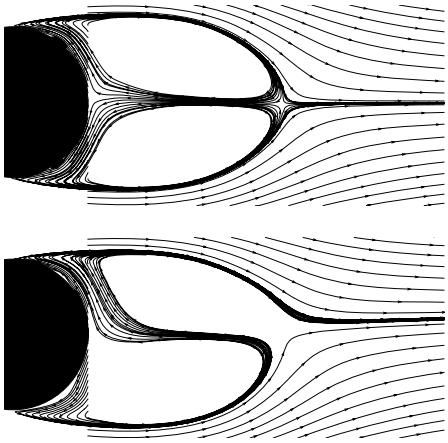

Figure 13: Pathlines of the mean velocity field for different shear rates (from the top: $SR = 0$ and 0.177)

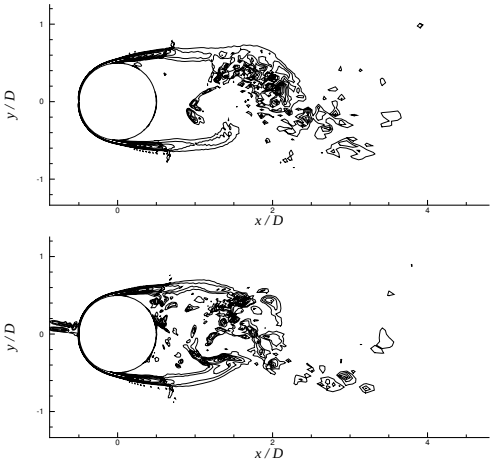

Figure 14: Spanwise vortex structures in the near wake: 11 contours of instantaneous vorticity magnitude between $|\omega_z|D/U_\infty = 2.5$ and $|\omega_z|D/U_\infty = 10.0$

Further illustration of the mean shear influence on the coherent structures in the cylinder wake is given in Fig. 15, where the iso-surfaces of the pressure fluctuations at one instant were compared for three shear rates. The level of each iso-surface was common for all three cases. Note the inclined x-axis. Regions of alternating, regularly located negative and positive pressure regions, which indicate the existence of the Kármán vorticies can be seen in all three cases. However, the vortex formation doesn't follow a staggered arrangement on both sides of the cylinder at the highest shear rate, in contrast to the other two cases. Here, the vorticies are observed only on the high velocity side. Regardless of the level of the iso-surface, no coherent structures on the low velocity side were recognized. In the case of higher shear rates, the vorticies are well preserved even in the far wake region. The convection into the positive y direction is clearly intensified.

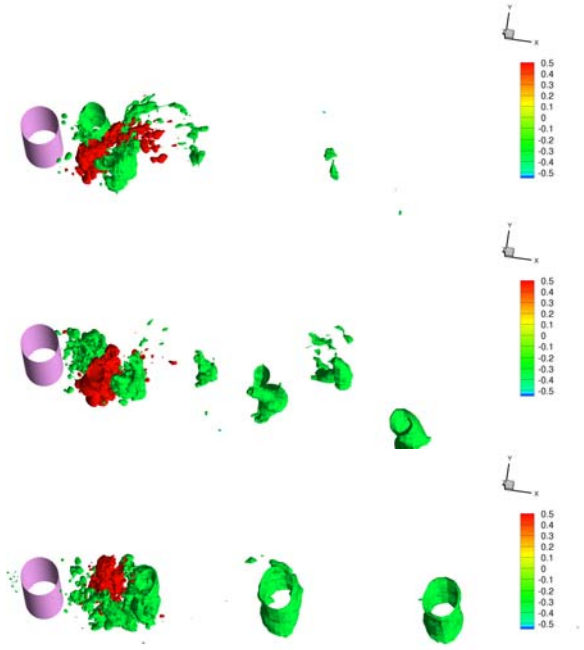

Figure 15: Isosurfaces (three levels) of the pressure fluctuation (From the top: $Sr = 0,\ 6.53 \cdot 10^{-4},\ 1.77 \cdot 10^{-1}$)

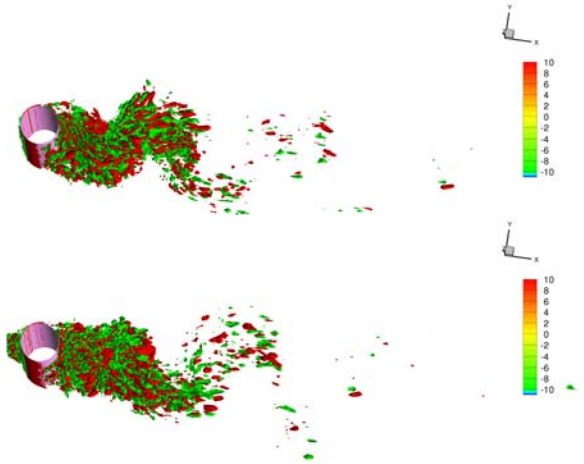

Figure 16: Isosurfaces (two levels) of Q (From the top: $SR = 0$ and 0.177)

The vortex structure is further represented by means of the Q-criteria ($Q = 0.5\,(\Omega_{ij}\Omega_{ij} - S_{ij}S_{ij})$), Fig. 16, with which the influence of the mean shear imposed on inflow on the small scales in the wake can be investigated. As illustrated in Fig. 16, the small vortical structures connecting the large scale vorticies, exhibit no significant differences between the shearless and sheared cases. It can be inferred that the small scale motion in the wake is less affected by the mean shear than the large scale motion, the latter observation being reflected in the mean velocities and the second moments. The spanwise length scale of the structures in the near wake is typically one fourth to one third of the cylinder diameter, which is in good agreement with the experimental and numerical observations found in the open literature, see e.g., the works of Kravchenko and Moin, 2000; Mansy et al., 1994 and Williamson, 1996.

CONCLUSIONS

Turbulent flow past a circular cylinder subjected to uniform mean shear at Reynolds number $Re_D = 3900$ was studied computationally by means of Large Eddy Simulation (LES) in the range of shear rates SR between 0 and 0.177. Special attention was devoted to the wake structure. In the very near wake, the inlet mean shear caused the entrainment of the fluid elements into the recirculation bubble on the low velocity side. This process is responsible for the pressure loss reduction, but the turbulence statistics remain almost unaffected in this flow region. The symmetric profile shapes were preserved. In the far wake, in contrast, the mean flow statistics were shifted to the high velocity side by increasing the shear rate. The strongest influence of the mean shear was observed at the profiles of the turbulent shear stress, whose energy budget exhibits an asymmetrical distribution, promoting the asymmetry of the normal turbulent stress components and formation of coherent structures on the high velocity side.

Acknowledgement

The financial support of the German Academic Exchange Service (DAAD) for T. Omori is gratefully acknowledged.

REFERENCES

Basara, B., Jakirlic, S. and Alajbegovic, A., 2003, "A T-RANS Study of a Shear Flow around Circular Cylinder Pertaining to Disperse Phase in Solid/Liquid Upward Duct Flow", *Turbulence, Heat and Mass Transfer*, Vol. 4, Begell House Inc., Hanjalic et al. (Eds.), pp. 1055-1062.

Breuer, M., 1998, "Large eddy simulation of the subcritical flow past a circular cylinder: numerical and modeling aspects", *Int. J. Num. Meth. in Fluids*, Vol. 28, p. 1281.

Germano, M., Piomelli, U., Moin, M. and Cabot, W. H., 1991, "A dynamic subgrid-scale eddy viscosity model", *Phys. Fluids A*, Vol. 3(7), pp. 1760-1765.

Hinze, J.O., 1959, "Turbulence", McGraw Hill, NY.

Kravchenko, A.G. and Moin, P., 2000, "Numerical studies of flow over a circular cylinder at ReD = 3900", *Phys. Fluids*, Vol. 12(2), pp. 403-417.

Legendre, D. and Magnaudet J., 1997, "A note on the lift force on a bubble or a drop in a low-Reynolds-number shear flow", *Phys. Fluids*, Vol. 9, pp. 3572–3574.

Lilly, D.K., 1992, "A proposed modification of the Germano subgrid-scale closure method", *Phys. Fluids A*, Vol. 4(3), pp. 633-635.

Mansy, H., Yang, P.M. and Williams, D.R., 1994, "Quantitative measurements of three-dimensional structures in the wake of a circular cylinder", *J. Fluid Mech.*, Vol. 270, pp. 277-296.

Mason, P.J. and Callen, N.S., 1985, "On the magnitude of the subgrid-scale eddy coefficient in large-eddy simulation of turbulent channel flow", *J. Fluid Mech.*, Vol. 162.

Moraga, F.J., Bonetto, F.J. and R.T. Lahey, R.T., 1999, "Lateral forces on spheres in turbulent uniform shear flow", *Int. J. Multiphase Flow*, Vol. 25.

Omori, T., Jakirlic, S., Tropea, C. and Obi, S., 2007, "Computational analysis of the shear-induced lift force on a cylindrical particle by means of LES with relevance to particle-laden liquid flow in an upward duct", 6th Int. Conf. on Multiphase Flow, Leipzig, Germany, July 9-13.

Piomelli, U. and Chasnov, J., 1996, "Large-eddy simulations: theory and applications", Kluwer Acad. Publisher.

Pope, S.B., 2000, "Turbulent flows", Cambridge University Press, Cambridge, U.K..

Travin, A., Shur, M., Strelets, M. and Spalart, P., 1999, "DES Past a Circular Cylinder", *Flow Turbulence and Combustion*, Vol. 63, pp. 293-313.

Williamson, C.H.K., 1996, "Vortex Dynamics in the Cylinder Wake", *Annu. Rev. Fluid. Mech.*, Vol. 28.